Research Article

Nano Research
2022, 15(8): 7026–7033

ISSN 1998-0124 CN 11-5974/O4
https://doi.org/10.1007/s12274-022-4344-0

Nanoporous $MoO_{3-x}/BiVO_4$ photoanodes promoting charge separation for efficient photoelectrochemical water splitting

Songcan Wang (✉), Boyan Liu, Xin Wang, Yingjuan Zhang, and Wei Huang (✉)

Frontiers Science Center for Flexible Electronics, Xi'an Institute of Flexible Electronics (IFE), Xi'an Institute of Biomedical Materials & Engineering, Northwestern Polytechnical University, Xi'an 710072, China

Received: 6 February 2022 / **Revised:** 16 March 2022 / **Accepted:** 18 March 2022

ABSTRACT

Owing to the relatively short hole diffusion length, severe charge recombination in the bulk of bismuth vanadate ($BiVO_4$) is the key issue for photoelectrochemical water splitting. Herein, we design a nanoporous $MoO_{3-x}/BiVO_4$ heterojunction photoanode to promote charge separation. The efficient electron transport properties of oxygen deficient MoO_{3-x} and the nanoporous structure are beneficial for charge separation, leading to a significantly enhanced PEC performance. The optimized $MoO_{3-x}/BiVO_4$ heterojunction photoanode exhibits a photocurrent density of 5.07 mA·cm^{-2} for Na_2SO_3 oxidation. By depositing FeOOH/NiOOH dual oxygen evolution cocatalysts to promote surface kinetics, a high photocurrent density of 4.81 mA·cm^{-2} can be achieved for PEC water splitting, exhibiting an excellent applied bias photon-to-current efficiency of 1.57%. Moreover, stable overall water splitting is achieved under consecutive light illumination for 10 h. We provide a proof of concept for the design of efficient $BiVO_4$-based heterojunction photoanodes for stable PEC water splitting.

KEYWORDS

water splitting, bismuth vanadate, heterojunction, oxygen vacancies, charge separation

1 Introduction

Bismuth vanadate ($BiVO_4$) has attracted great attention as a promising photoanode material for photoelectrochemical (PEC) water splitting due to its narrow bandgap (2.4 eV) for visible light absorption, suitable band edge positions for water oxidation, relatively good stability in aqueous solutions, and low cost [1–4]. Based on the bandgap of 2.4 eV, the theoretical maximum photocurrent density of $BiVO_4$ under air mass (AM) 1.5 G illumination is as high as 7.5 mA·cm^{-2}, corresponding to a solar-to-hydrogen (STH) conversion efficiency of 9.2% [5]. However, the hole diffusion length of $BiVO_4$ is only around 70 nm [6], leading to poor charge transport and separation properties within the film. Consequently, the actual photocurrent densities achieved for pristine $BiVO_4$ photoanodes are much lower than the theoretical value. Since charge separation efficiency in a photoanode determines the number of photogenerated holes reaching the photoanode/ electrolyte interface for oxygen evolution reaction (OER), the development of proper strategies to promote charge separation is essential to achieve a high PEC performance.

Generally, reducing the film thickness of a $BiVO_4$ photoanode can shorten the carrier transport distance, and thus a higher charge separation efficiency can be achieved. However, a relatively thick film is required to guarantee sufficient light absorption. To achieve a high charge separation efficiency in a relatively thick $BiVO_4$ film, various strategies such as the formation of nanoporous structure [7–9], crystal facet engineering [10–13], creation of oxygen vacancies [14–16], elemental doping [17–19], and heterojunction construction [20–23] have been developed in the past decades. In particular, the formation of $WO_3/BiVO_4$ heterojunction has been confirmed as a great success to achieve excellent PEC performance [24–26]. This is because WO_3 has a carrier mobility of 12 cm^2·V^{-1}·s^{-1} [27, 28], which is at least two orders of magnitude higher than that of $BiVO_4$ (0.044 cm^2·V^{-1}·s^{-1}) [6]. In addition, the band structure of WO_3 is matchable with $BiVO_4$, which can form a type-II heterojunction that promotes the separation of photogenerated electrons and holes [29]. Based on the above analysis, it is reasonable to deduce that other semiconductors with higher carrier mobility and suitable band structure can be coupled with $BiVO_4$ to form a type-II heterojunction to improve its charge separation efficiency.

Owing to the intrinsic wide bandgap (> 2.7 eV), the carrier concentration of MoO_3 is low that hinders its application for electronic devices [30]. Interestingly, the electrical conductivity of MoO_3 can be significantly improved by the formation of oxygen vacancies. For example, few-layer MoO_{3-x} with enriched oxygen vacancies exhibits ultrahigh mobility (> 1,100 cm^2·V^{-1}·s^{-1}) [31], which is two orders of magnitude higher than that of WO_3. Therefore, electron transport in MoO_{3-x} should be much faster than in WO_3, which is beneficial for charge separation. Considering that the bandgaps of MoO_{3-x} and WO_3 are similar, and the work function of MoO_{3-x} (6.6 eV) is similar to that of WO_3 (6.3–6.7 eV) [32–34], the band alignment between $BiVO_4$ and MoO_{3-x} should also be similar to that between $BiVO_4$ and WO_3. Thus, proper design of the $MoO_{3-x}/BiVO_4$ heterojunction may potentially achieve a new breakthrough in the PEC performance.

Herein, we develop a hydrothermal process to *in-situ* covert

Address correspondence to Songcan Wang, iamscwang@nwpu.edu.cn; Wei Huang, iamwhuang@nwpu.edu.cn

electrodeposited BiOI nanosheet arrays into Bi_2MoO_6 nanosheet arrays, followed by calcination with vanadyl acetylacetonate ($VO(C_5H_7O_2)_2$). After removing the excess V_2O_5, a nanoporous $MoO_{3-x}/BiVO_4$ heterojunction film can be obtained. The film thickness can be tuned by changing the electrodeposition time of the BiOI nanosheet arrays. The optimized $MoO_{3-x}/BiVO_4$ photoanode with surface deposition of FeOOH/NiOOH dual cocatalysts exhibits an excellent photocurrent density of 4.81 $mA·cm^{-2}$ at 1.23 V vs. the reverse hydrogen electrode (RHE) under AM 1.5 G illumination, delivering an applied bias photon-to-current efficiency (ABPE) of 1.57%. In addition, the obtained $MoO_{3-x}/BiVO_4$/FeOOH/NiOOH photoanode can achieve stable overall water splitting under consecutive light illumination for 10 h. This work demonstrates the possibility of using $MoO_{3-x}/BiVO_4$ heterojunctions as efficient photoanodes for PEC water splitting.

2 Experimental

2.1 Preparation of BiOI films

BiOI films were prepared by a typical three-electrode electrochemical deposition method with fluorine-doped tin oxide (FTO) substrates (1.5 cm × 2.0 cm) as the working electrode, Pt wire as the counter electrode, and saturated Ag/AgCl as the reference electrode according to a previous report with some modifications [8]. The BiOI precursor solution was prepared by dissolving 0.04 M $Bi(NO_3)_3·5H_2O$ (Sigma–Aldrich, ≥ 98.0%) in 50 mL of 0.40 M potassium iodide (KI, Sigma–Aldrich, ≥ 99.5%) solution with a pH adjusted to 1.7 by HNO_3. The obtained solution was mixed with 0.23 M p-benzoquinone (Sigma–Aldrich, ≥ 98%) dissolved in 20 mL of ethanol. Electrodeposition was carried out at −0.1 V vs. Ag/AgCl for 1–5 min at room temperature. The obtained BiOI films with different electrodeposited time were rinsed with deionized water and denoted as BOI-*x* (*x* refers to the electrodeposited time of 1, 3 and 5 min).

2.2 Preparation of Bi_2MoO_6 films

The BOI-*x* films were immerged in 15 mL of 0.1 M $(NH_4)_6Mo_7O_{24}·4H_2O$ solution and transferred to a Teflon–lined stainless autoclave, which was placed in an oven at 180 °C for 8 h. After cooling down to room temperature, the samples were rinsed with deionized water and dried in air. The obtained samples were denoted as BMO-*x* (*x* refers to the electrodeposited time of 1, 3 and 5 min for the BOI precursor films).

2.3 Preparation of $MoO_{3-x}/BiVO_4$ films

0.1 mL of 0.2 M $VO(C_5H_7O_2)_2$ dissolved in methanol was placed on the surface of the obtained BMO-*x* films. After the methanol was evaporated, the films were annealed in a muffle furnace at 500 °C for 2 h. Then, the films were immerged in 1 M KOH (Sigma–Aldrich, ≥ 90.0%) solution for 30 min to remove the excess V_2O_5. After rinsing with deionized water and drying in air, the obtained $MoO_{3-x}/BiVO_4$ films were denoted as MO/BVO-*x* (*x* refers to the electrodeposited time of 1, 3, and 5 min for the BOI precursor films). For comparison, another BOI-3 film was also treated with $VO(C_5H_7O_2)_2$ under the same conditions shown above, and the converted sample was denoted as BVO-3.

2.4 Cocatalyst deposition on the $MoO_{3-x}/BiVO_4$ films

The FeOOH/NiOOH cocatalysts were deposited using a photo-assisted electrodeposition (PED) process under AM 1.5 G illumination according to a previous report with some modification [8]. Briefly, FeOOH was deposited from a 0.1 M $Fe(SO_4)_2·7H_2O$ (Sigma–Aldrich, 99%) solution previously purged with N_2 for 20 min at 0.25 V vs. Ag/AgCl. Then, NiOOH was deposited from a 0.1 M $Ni(SO_4)_2·6H_2O$ (Sigma–Aldrich, 99%) solution (pH = 7.0, adjusting by 0.1 M KOH) at 0.11 V vs. Ag/AgCl. To achieve the optimized PEC performance, the deposition times for FeOOH and NiOOH were 15 and 5 min, respectively. For both cocatalysts, after the PED process, additional electrodeposition was conducted in the same solution for 1 min in the dark to completely cover the possible pinholes in the films.

2.5 Characterizations

Morphologies and crystal structures of the films were characterized by field emission scanning electron microscopy (FESEM, JSM-7100F, JEOL), transmission electron microscopy (TEM, F20 FEG-STEM, FEI), and X-ray diffraction (XRD, D8 Advance, Bruker) with Cu Kα (λ = 0.15406 nm) radiation, respectively. The surface chemical states and composition of the films were characterized by X-ray photoelectron spectroscopy (XPS) with an Al Kα ($h\nu$ = 1,253.6 eV) radiation source. All the binding energies were calibrated using C 1s (284.8 eV) as the reference. Ultraviolet–visible (UV–Vis) absorption spectra of the films were obtained on a spectrophotometer (UV-2600i, Shimadzu).

2.6 Photoelectrochemical performances

PEC performances of the obtained films was measured using a typical three-electrode cell with a Xe 150 W lamp as the light source. Light was illuminated through an AM 1.5 G filter and the light intensity was carefully calibrated to ca. 100 $mW·cm^{-2}$ by a thermopile optical detector (Beijing China Education Au-Light Co., Ltd.). A platinum wire and an Ag/AgCl (saturated KCl) electrode were used as the counter electrode and reference electrode, respectively. A 1 M borate buffer solution was prepared by dissolving 0.1 mol of H_3BO_3 (Sigma–Aldrich, 99.5%) in 100 mL of Milli-Q water, followed by adding KOH (Sigma–Aldrich, 90%) to achieve a pH of 7, which was then used as the electrolyte for all PEC measurements, while the charge separation efficiencies of the films were measured in the presence of 0.2 M Na_2SO_3 by keeping the pH at 7. Photocurrent–potential curves were obtained using linear sweep voltammetry (LSV) in a voltage window of 0.1–1.3 V vs. RHE with a scan rate of 50 mV s^{-1} on an electrochemical workstation (CHI700e, CH Instruments, Inc.). Long-term stability of the photoanode was evaluated at 1.23 V vs. RHE under AM 1.5 G illumination for 10 h. To evaluate the overall water splitting performance, the photocurrent densities of the $MoO_{3-x}/BiVO_4$/FeOOH/NiOOH films were measured in an air-tight cell at 1.23 V vs. RHE under AM 1.5 G illumination for 10 h and the number of gases was detected with a gas chromatograph (Beijing China Education Au-Light Co., Ltd., GC-7920) every 2 h.

3 Results and discussion

The preparation of $MoO_{3-x}/BiVO_4$ heterojunction films was schematically illustrated in Fig. 1(a). BiOI films were prepared according to a previous report with some modifications [8]. The film thickness was tailored by changing the electrodeposition time, and the obtained samples were denoted as BOI-*x* (*x* refers to the electrodeposition time of 1, 3, and 5 min). As shown in Figs. 1(b)–1(d), BiOI nanosheet arrays with a film thickness from 200 to 600 nm can be achieved by changing the electrodeposition time from 1 to 5 min. However, the sizes of the nanosheets are similar. XRD patterns shown in Fig. 1(e) reveal that along with the FTO signals, all peaks can be assigned to BiOI (PDF#10-0445) [35]. Interestingly, after hydrothermal treating the BOI-*x* films with a $(NH_4)_6Mo_7O_{24}·4H_2O$ solution, the nanosheet array structures can

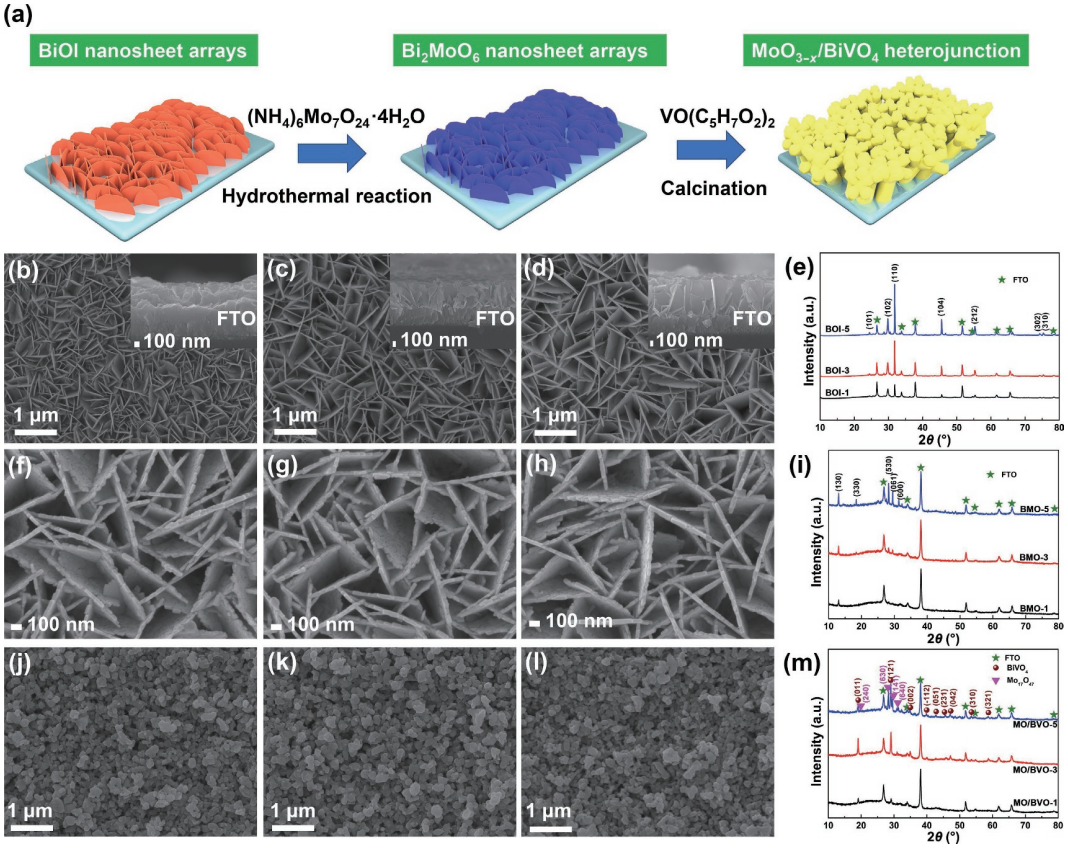

Figure 1 (a) Schematic illustration for the preparation of $MoO_{3-x}/BiVO_4$ heterojunction films. SEM images of (b) BOI-1, (c) BOI-3, and (d) BOI-5. Insets in (b)–(d): the corresponding cross-sectional views. (e) XRD patterns of BOI-1, BOI-3, and BOI-5. SEM images of (f) BMO-1, (g) BMO-3, and (h) BMO-5. (i) XRD patterns of BMO-1, BMO-3, and BMO-5. SEM images of (j) MO/BVO-1, (k) MO/BVO-3, and (l) MO/BVO-5. (m) XRD patterns of MO/BVO-1, MO/BVO-3, and MO/BVO-5.

be maintained (Figs. 1(f)–1(h)). According to the XRD patterns shown in Fig. 1(i), the BOI-*x* films have been successfully converted to Bi_2MoO_6 (PDF#33-0208, the corresponding samples were denoted as BMO-*x*) [36]. With the elongation of the electrodeposition time for BiOI precursor films, the XRD peaks of the converted Bi_2MoO_6 become stronger. We found that the $(NH_4)_6Mo_7O_{24}\cdot 4H_2O$ solution during hydrothermal reaction was essential to keep the nanosheet array structure for the obtained BMO-*x*. To investigate the effect of the molybdenum solution on the morphology of the obtained Bi_2MoO_6, another BOI-3 film was hydrothermally treated with a Na_2MoO_4 solution, and the obtained sample was denoted as BMO-3N. As shown in Fig. S1 in the Electronic Supplementary Material (ESM), BMO-3N exhibits a nanoplate array structure rather than the nanosheet array structure. The thickness of the nanoplate is approximately 90 nm. In addition, numerous nanoparticles attached on the nanoplates can be observed.

By dropping 70 μL of $VO(C_5H_7O_2)_2$ solution, the BMO-*x* films were annealed in a Muffle furnace at 500 °C for 2 h. After cooling down to room temperature, the excess amount of V_2O_5 was washed out with a NaOH solution. As revealed in the SEM images (Figs. 1(j)–1(l)), the nanosheet array structures disappeared and numerous nanoparticles ranging from 200 to 600 nm can be observed, which is beneficial for charge migration and transfer. According to the XRD patterns (Fig. 1(m)), both $BiVO_4$ and $Mo_{17}O_{47}$ signals can be observed [37, 38], indicating the formation of $Mo_{17}O_{47}/BiVO_4$ heterojunctions. With the increase of the electrodeposition time for the BiOI precursor films, the $Mo_{17}O_{47}$ peaks become stronger, indicating the formation of more $Mo_{17}O_{47}$. The formation of $Mo_{17}O_{47}$ with oxygen vacancies is beneficial for electron transport, which is expected to efficiently promote charge separation in the $Mo_{17}O_{47}/BiVO_4$ heterojunction.

To confirm the interfacial contact between $Mo_{17}O_{47}$ and $BiVO_4$, the MO/BVO-3 sample was scratched out from the MO/BVO-3 film, which was observed by high resolution transmission electron microscopy (HRTEM). Figure 2(a) shows a broken particle with a length of around 600 nm and a width of around 300 nm, which is consistent to the particle size shown in the SEM image (Fig. 1(k)). HRTEM image of the selective area (red square in Fig. 2(a)) demonstrates two different kinds of lattice fringes with a clear boundary (white dash line in Fig. 2(b)), which is the interface between $Mo_{17}O_{47}$ and $BiVO_4$. More specifically, the lattice fringe of 0.48 nm can be assigned to the *d*-spacing value of the (110) facet for $BiVO_4$ [39], whereas the lattice fringe of 0.36 nm corresponds to the *d*-spacing value of the (440) facet for $Mo_{17}O_{47}$. In addition, an amorphous-like area can be observed in the $Mo_{17}O_{47}$ part (red dash rectangle in Fig. 2(b)), which is due to the formation of oxygen vacancies [40].

To confirm the formation of heterojunction between $Mo_{17}O_{47}$ and $BiVO_4$, XPS was carried out to study the surface chemical composition of the MO/BVO-3 and BVO-3 photoanodes. As shown in Fig. 3(a), in addition to the Sn signals that is attributed to the FTO substrates, only Bi, V, and O signals can be observed for the BVO-3 sample. The MO/BVO-3 sample exhibits Mo signals, which is due to the presence of $Mo_{17}O_{47}$. It is obvious that the Bi 4f, V 2p, and O 1s peaks of MO/BVO-3 are all positively shifted to higher binding energy compared to those of BVO-3 (Figs. 3(b)–3(d)), which is due to the electron transfer from $BiVO_4$ to $Mo_{17}O_{47}$ at the interfaces [41]. Therefore, $Mo_{17}O_{47}$ and $BiVO_4$ can form a heterojunction to promote charge separation.

As shown in Fig. 3(c), along with the typical V $2p_{1/2}$ and V $2p_{3/2}$ peaks, a shoulder peak located at approximately 515.1 eV can be observed for BVO-3, which is a satellite peak for V 2p (denoted as V_{sat}), due to a strong hybridization between V 3d and O 2p levels [42]. Owing to the electron transfer from $BiVO_4$ to $Mo_{17}O_{47}$ at the interfaces, the V_{sat} peak for MO/BVO-3 is positively shifted to

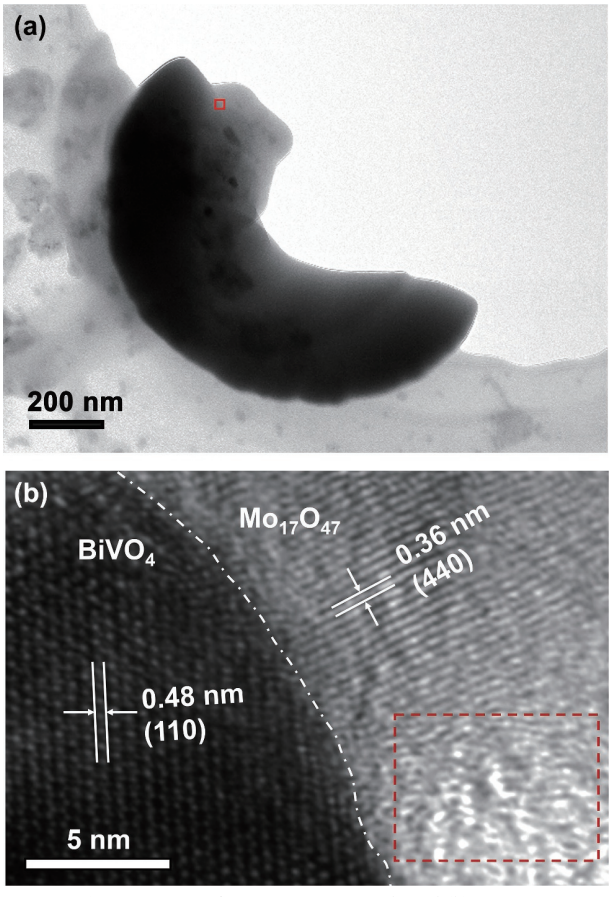

Figure 2 (a) TEM image of a MO/BVO-3 particle and (b) HRTEM image of the selective area (red square in (a)).

around 515.7 eV. In addition, the oxygen vacancy (O_v) characteristic peak can be observed in both MO/BVO-3 and BVO-3 (Fig. 3(d)), indicating the presence of oxygen vacancies, which is beneficial for charge separation [43]. As listed in Table S1 in the ESM, the surface O_v ratios of BVO-3 and MO/BVO-3 are 58.8% and 37.9%, respectively. It should be mentioned that this is only the surface chemical information, which may be different from that in the bulk of the samples. The Mo $3d_{3/2}$ peak of MO/BVO-3 can be deconvoluted into two peaks located at 236.3 and 235.7 eV (Fig. S2 in the ESM), corresponding to Mo^{6+} and Mo^{5+}, respectively [44]. It is obvious that the area of the Mo^{5+} peak is much larger than that of the Mo^{6+} peak, indicating that the surface of $Mo_{17}O_{47}$ is enriched with oxygen vacancies, which is consistent with the HRTEM results (Fig. 2(b)).

Charge separation properties of the obtained MO/BVO-1, MO/BVO-3, and MO/BVO-5 photoanodes were measured in a typical three-electrode system using 1 M KBi electrolyte in the presence of 0.2 M Na_2SO_3 as the sacrificial agent. Since the oxidation of SO_3^{2-} can consume all photogenerated holes reaching the photoanode/electrolyte interfaces [45], photocurrent densities of the samples reflect the charge separation efficiencies of the photoanodes. As shown in Fig. 4(a), the MO/BVO-1 photoanode exhibits a photocurrent density of 4.24 mA·cm^{-2} at 1.23 V vs. RHE under AM 1.5 G illumination, whereas the MO/BVO-3 photoanode can reach a photocurrent density of 5.07 mA·cm^{-2}. However, the photocurrent density of MO/BVO-5 photoanode decreases to 3.24 mA·cm^{-2} at 1.23 V vs. RHE under AM 1.5 G illumination. To confirm the MO/BVO-3 heterojunction for promoting charge separation, the PEC Na_2SO_3 oxidation performance of BVO-3 was also measured. The BVO-3 exhibits a typical nanoporous structure (Fig. S3(a) in the ESM), exhibiting a photocurrent density of 3.82 mA·cm^{-2} at 1.23 V vs. RHE under AM 1.5 G illumination (Fig. S3(b) in the ESM), which is only 75.3% that of its MO/BVO-3 counterpart. Therefore, the MO/BVO-3 heterojunction photoanode is efficient to promote charge separation.

To investigate the PEC water splitting performance, photocurrent densities of the MO/BVO-1, MO/BVO-3, and MO/BVO-5 photoanodes were also measured in 1 M KBi electrolyte without Na_2SO_3. As shown in Fig. 4(b), the MO/BVO-1 photoanode exhibits a photocurrent density of 1.38 mA·cm^{-2} at 1.23 V vs. RHE, while the MO/BVO-3 photoanode exhibits a higher photocurrent density of 2.21 mA·cm^{-2}. However, the MO/BVO-5 photoanode exhibits a decreased photocurrent density of 1.12 mA·cm^{-2}. Obviously, the photocurrent densities of

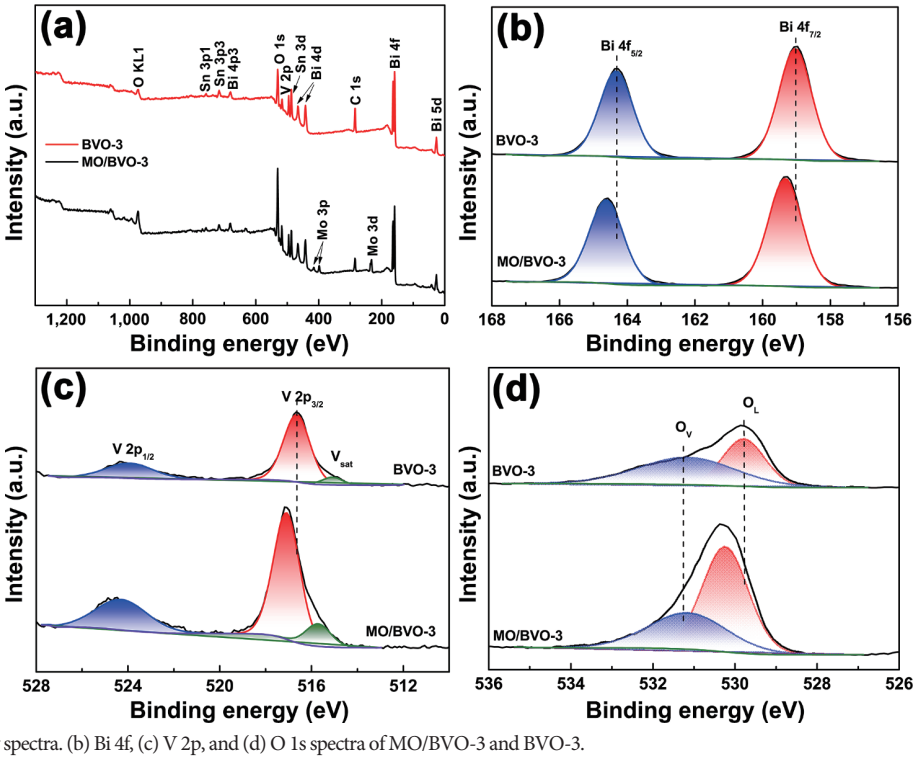

Figure 3 (a) XPS survey spectra. (b) Bi 4f, (c) V 2p, and (d) O 1s spectra of MO/BVO-3 and BVO-3.

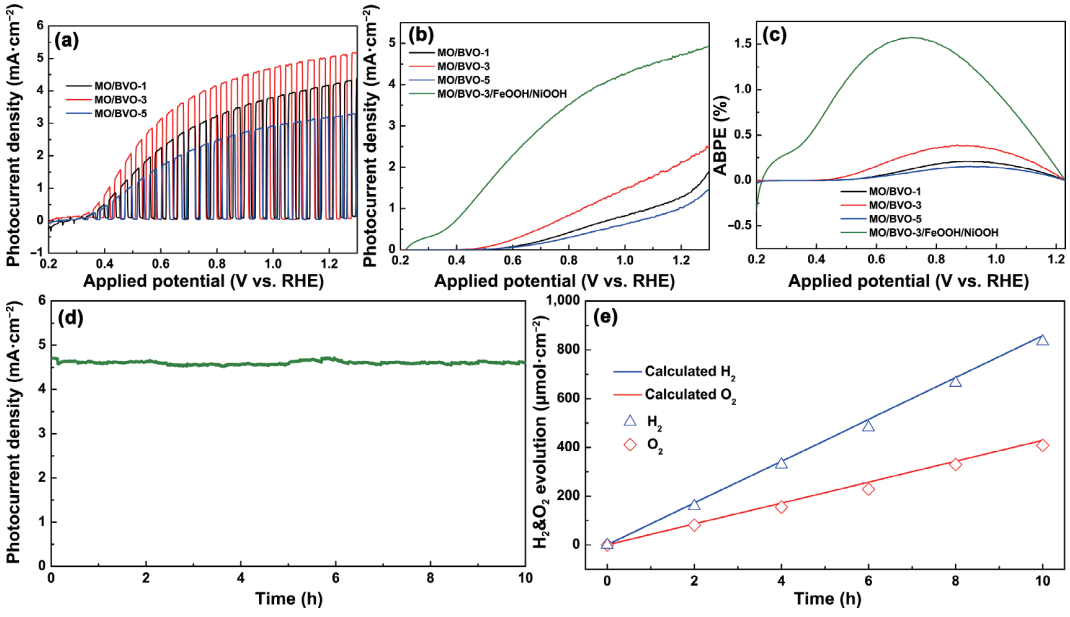

Figure 4 (a) Photocurrent density vs. potential of the MO/BVO-1, MO/BVO-3, and MO/BVO-5 photoanodes in a 1 M borate buffer electrolyte containing 0.2 M Na_2SO_3 under AM 1.5 G illumination. (b) Photocurrent density vs. potential and (c) ABPE curves of the MO/BVO-1, MO/BVO-3, MO/BVO-5, and MO/BVO-3/FeOOH/NiOOH photoanodes in a 1 M borate buffer electrolyte under AM 1.5 G illumination. (d) *J*–*t* curve of the MO/BVO-3/FeOOH/NiOOH photoanode at 1.23 V vs. RHE under AM 1.5 G illumination in a 1 M borate buffer electrolyte. (e) Gas evolution from PEC water splitting of the MO/BVO-3/FeOOH/NiOOH photoanode at 1.23 V vs. RHE under AM 1.5 G illumination.

all samples measured in the presence of Na_2SO_3 are much higher, indicating that oxygen evolution cocatalysts (OECs) are required to accelerate OER at the photoanode/electrolyte interfaces. By depositing approximately 10 nm of a FeOOH/NiOOH ultrathin layer as the dual OECs for the MO/BVO-3 photoanode (Fig. S4 in the ESM), the obtained MO/BVO-3/FeOOH/NiOOH photoanode exhibits a significantly enhanced photocurrent density of 4.81 mA·cm^{-2}. The ABPE values of the MO/BVO-1, MO/BVO-3, MO/BVO-5, and MO/BVO-3/FeOOH/NiOOH photoanodes were calculated according to Eq. (S2) in the ESM. As shown in Fig. 4(c), the MO/BVO-1 photoanode exhibits a very low ABPE of 0.21% at around 0.90 V vs. RHE, while the MO/BVO-3 photoanode shows a much higher ABPE of 0.38%. In comparison, the MO/BVO-5 photoanode exhibits the lowest ABPE of 0.15%. With the deposition of FeOOH/NiOOH dual OECs to promote surface OER, the MO/BVO-3/FeOOH/NiOOH photoanode exhibits a much higher ABPE of 1.57% at a lower applied potential of 0.71 V. Therefore, FeOOH/NiOOH dual OECs are efficient to promote OER.

Long-term stability of the MO/BVO-3/FeOOH/NiOOH photoanode was measured at 1.23 V vs. RHE under AM 1.5 G illumination for 10 h. As shown in Fig. 4(d), the photoanode exhibits a high photocurrent density of around 4.8 mA·cm^{-2}, which is very stable under consecutive illumination for 10 h. To demonstrate the overall water splitting performance, the MO/BVO-3/FeOOH/NiOOH photoanode was applied as the working electrode in an air-tight cell using Pt as the counter electrode and Ag/AgCl electrode as the reference electrode. The produced gases were measured every 2 h. As shown in Fig. 4(e), 834.2 μmol·cm^{-2} of hydrogen and 407.8 μmol·cm^{-2} of oxygen can be generated in 10 h at 1.23 V vs. RHE under AM 1.5 G illumination, which is close to the 2:1 ratio for the water splitting reaction. The Faradaic efficiency for oxygen evolution is around 95.1%.

To understand the underlying mechanism for the improved PEC performances, the optoelectrical properties of the MO/BVO-1, MO/BVO-3, MO/BVO-5, and MO/BVO-3/FeOOH/NiOOH photoanodes were studied. As shown in Fig. 5(a), the MO/BVO-1 photoanode exhibits a light absorption edge at around 500 nm, while the light absorption edge of the MO/BVO-3 and MO/BVO-5 photoanodes are decreased to approximately 490 nm. According to the UV–Vis light absorption curves, the bandgaps of the MO/BVO-1, MO/BVO-3, and MO/BVO-5 photoanodes were calculated to be 2.51, 2.53, and 2.58 eV, respectively (Fig. 5(b)). It should be mentioned that the bandgaps of all samples are larger than that of BVO-3 (Fig. S5 in the ESM), which is due to the incorporation of MoO_{3-x} that has a larger bandgap than $BiVO_4$. Incident-photon-to-current conversion efficiency (IPCE) curves of the MO/BVO-1, MO/BVO-3, MO/BVO-5, and MO/BVO-3/FeOOH/NiOOH photoanodes were measured in a 1 M borate buffer electrolyte at 1.23 V vs. RHE under AM 1.5 G illumination. As shown in Fig. 5(c), the MO/BVO-1 photoanode exhibits a maximum IPCE value of 30.1% at 400 nm, whereas a much higher IPCE value of 56.7% is achieved for the MO/BVO-3 photoanode. The MO/BVO-5 photoanode shows the lowest IPCE value 26.5%. As expected, the MO/BVO-3/FeOOH/NiOOH photoanode exhibits a high IPCE value of approximately 85%. These results confirm that the MO/BVO-3 photoanode is efficient to enhance the charge separation efficiency in the bulk, but severe charge recombination still occurs at the photoanode/electrolyte interfaces. With the deposition of FeOOH/NiOOH dual OECs, the surface charge transfer efficiency can be significantly improved, resulting in the much higher IPCE values and photocurrent densities.

To understand the interfacial kinetics during OER, electrochemical impedance spectroscopy (EIS) curves of the MO/BVO-1, MO/BVO-3, and MO/BVO-5 photoanodes were measured at the open circuit potential under AM 1.5 G illumination. As shown in Fig. 5(d), all three films exhibit a typical EIS curve consisting of only one semicircle, and an equivalent circuit model (inset in Fig. 5(d)) consisting of a series resistance (R_s), a charge transfer resistance (R_{ct}), and a constant phase angle element (CPE) is employed to gain more insights of the EIS results [46]. Generally, R_{ct} reflects the OER kinetics at the photoanode/electrolyte interfaces. As listed in Table S2 in the ESM, R_{ct} values of the MO/BVO-1, MO/BVO-3, and MO/BVO-5 photoanodes are 560.1, 441.2, and 708.2 Ω, respectively. Therefore, the electron transfer at the MO/BVO-3 surface is faster than that

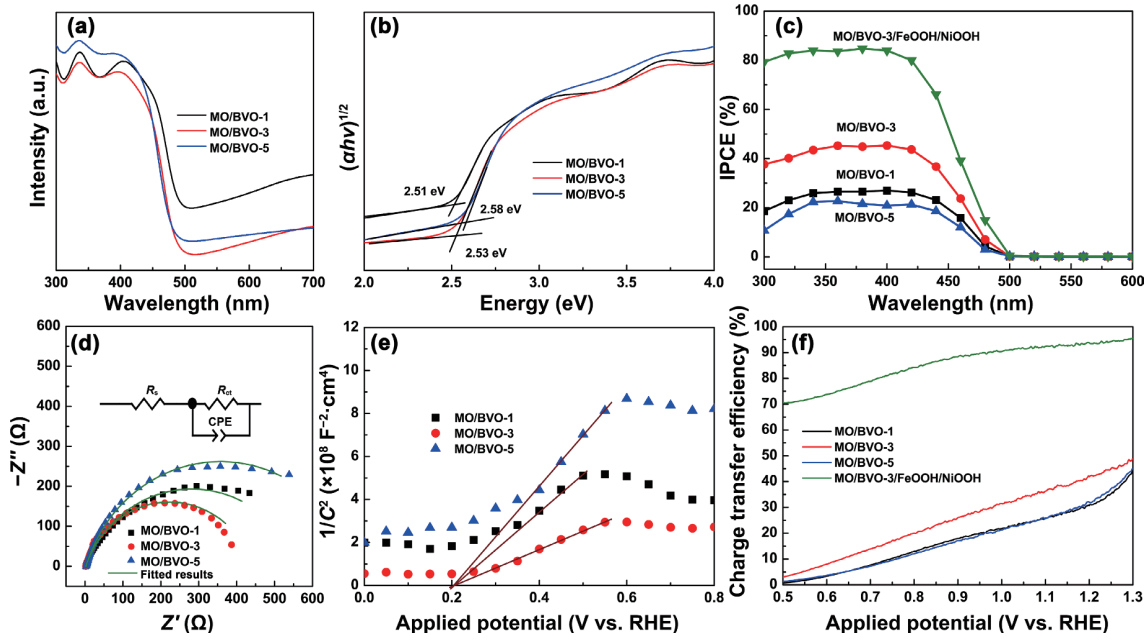

Figure 5 (a) UV–Vis absorption curves and (b) estimated bandgaps of MO/BVO-1, MO/BVO-3, and MO/BVO-5. (c) IPCE curves of MO/BVO-1, MO/BVO-3, MO/BVO-5, and MO/BVO-3/FeOOH/NiOOH. (d) EIS plots and (e) MS curves of MO/BVO-1, MO/BVO-3, and MO/BVO-5. (f) Charge transfer efficiencies of MO/BVO-1, MO/BVO-3, MO/BVO-5, and MO/BVO-3/FeOOH/NiOOH. Inset in (d): the equivalent circuit model.

in the MO/BVO-1 and MO/BVO-5 photoanodes.

To gain more insight of the electronic properties, Mott–Schottky (MS) curves of the MO/BVO-1, MO/BVO-3, and MO/BVO-5 photoanodes were measured in a 1 M borate buffer electrolyte (pH 9.5) under darkness. As shown in Fig. 5(e), all samples exhibit a positive slope in the MS curves, indicating the n-type characteristics [47]. Moreover, the MO/BVO-3 photoanode exhibits the smallest slope among all samples, suggesting that the MO/BVO-3 photoanode has the highest charge carrier density. According to Eq. (S4) in the ESM, carrier densities of the MO/BVO-1, MO/BVO-3, and MO/BVO-5 photoanodes were calculated. As listed in Table S3 in the ESM, the carrier density of the MO/BVO-3 photoanode is 2.47×10^{19} cm^{-3}, which is around 2 and 2.8 times higher than that of MO/BVO-1 and MO/BVO-5 photoanodes, respectively. Thus, the electronic conductivity of the MO/BVO-3 photoanode is better than the other samples, leading to better electron-hole separation, which is consistent with the photocurrent densities shown in Fig. 4(a).

According to Eq. (S5) in the ESM, the surface charge transfer efficiency (η_{trans}) values for the MO/BVO-1, MO/BVO-3, MO/BVO-5, and MO/BVO-3/FeOOH/NiOOH photoanodes at different applied potentials were calculated. As shown in Fig. 5(f), the MO/BVO-3 photoanode exhibits a higher η_{trans} value of 43.3% at 1.23 V vs. RHE comparted to that of the MO/BVO-1 and MO/BVO-5 photoanodes. With the surface deposition of FeOOH/NiOOH dual OECs, the MO/BVO-3/FeOOH/NiOOH photoanode exhibits a much higher η_{trans} of 93.6% at 1.23 V vs. RHE, implying that the FeOOH/NiOOH dual OECs can efficiently promote surface charge transfer from the photoanode to the electrolyte for OER.

We further found that our strategy can also be applied for the preparation oxygen deficient $WO_{3-x}/BiVO_4$ heterojunction photoanodes to boost the PEC performance. As shown in Fig. S6(a) in the ESM, the nanosheet arrays can be maintained after hydrothermally treating the BOI-3 film with a Na_2WO_4 solution. The XRD pattern confirms the successful formation of Bi_2WO_6 (Fig. S6(b) in the ESM) [48]. After annealing the obtained Bi_2WO_6 film with $VO(C_5H_7O_2)_2$ and the subsequent removal of excess V_2O_5, nanoparticles with a size of 200–400 nm can be observed (Fig. S6(c) in the ESM). As revealed in the XRD pattern (Fig. S6(d) in the ESM), the obtained film is composed of oxygen deficient $WO_{2.92}$ and $BiVO_4$. The obtained $WO_{2.92}/BiVO_4$ film (denoted as WO/BVO-3) exhibits a photocurrent density of 4.53 mA·cm^{-2} at 1.23 V vs. RHE under AM 1.5 G illumination for Na_2SO_3 oxidation (Fig. S7 in the ESM), which is higher than its BVO-3 counterpart (Fig. S3 in the ESM). Therefore, our strategy of using a Bi_2MO_6 (M = Mo, W) precursor film to form oxygen deficient $MO_{3-x}/BiVO_4$ heterojunction film may be applicable for the design of other efficient photoanodes for PEC water splitting.

4 Conclusions

In conclusion, we have reported a $MoO_{3-x}/BiVO_4$ heterojunction that can efficiently promote charge separation. The formation of oxygen vacancies in MoO_{3-x} can improve the electron mobility, providing an electron "highway" for charge separation and transport in the $MoO_{3-x}/BiVO_4$ heterojunction. The content of MoO_{3-x} can be tailored by tuning the electrodeposition time of the BiOI precursor films. The optimized $MoO_{3-x}/BiVO_4$ heterojunction photoanode exhibits a nanoporous structure, which is efficient to promote charge separation, exhibiting a high photocurrent density of 5.07 mA·cm^{-2} at 1.23 V vs. RHE under AM 1.5 G illumination in the presence of Na_2SO_3 as the hole sacrificial agent. By depositing FeOOH/NiOOH dual OECs to accelerate the surface reaction kinetics for OER, the optimized $MoO_{3-x}/BiVO_4$/FeOOH/NiOOH photoanode can achieve a photocurrent density of 4.81 mA·cm^{-2} and a high ABPE of 1.57% for PEC water splitting. Stable overall water splitting is realized for 10 h. This work provides a rational strategy for the design of $MoO_{3-x}/BiVO_4$ heterojunction photoanodes to promote charge separation, providing an alternative avenue for efficient PEC water splitting.

Acknowledgements

The authors would like to acknowledge the financial support from the National Natural Science Foundation of China (No. 52002328), the Fundamental Research Funds for the Central Universities, the Joint Research Funds of Department of Science & Technology of Shaanxi Province, and Northwestern Polytechnical

University (No. 2020GXLH-Z-018).

Electronic Supplementary Material: Supplementary material (detailed equations; SEM images; XPS; PEC performance, TEM image, the Kubelka–Munk function vs. the energy spectrum; XRD patterns; EIS fitted results; Carrier densities) is available in the online version of this article at https://doi.org/10.1007/s12274-022-4344-0.

References

[1] Kim, J. H.; Lee, J. S. Elaborately modified $BiVO_4$ photoanodes for solar water splitting. *Adv. Mater.* **2019**, *31*, 1806938.

[2] Park, Y.; McDonald, K. J.; Choi, K. S. Progress in bismuth vanadate photoanodes for use in solar water oxidation. *Chem. Soc. Rev.* **2013**, *42*, 2321–2337.

[3] Wang, L.; Zhang, T.; Su, J. Z.; Guo, L. J. Room-temperature photodeposition of conformal transition metal based cocatalysts on $BiVO_4$ for enhanced photoelectrochemical water splitting. *Nano Res.* **2020**, *13*, 231–237.

[4] Kang, Y. Y.; Chen, R.; Zhen, C.; Wang, L. Z.; Liu, G.; Cheng, H. M. An integrated thermoelectric-assisted photoelectrochemical system to boost water splitting. *Sci. Bull.* **2020**, *65*, 1163–1169.

[5] Wang, S. C.; Wang, L. Z.; Huang, W. Bismuth-based photocatalysts for solar energy conversion. *J. Mater. Chem. A* **2020**, *8*, 24307–24352.

[6] Abdi, F. F.; Savenije, T. J.; May, M. M.; Dam, B. Van De Krol, R. The origin of slow carrier transport in $BiVO_4$ thin film photoanodes: A time-resolved microwave conductivity study. *J. Phys. Chem. Lett.* **2013**, *4*, 2752–2757.

[7] McDonald, K. J.; Choi, K. S. A new electrochemical synthesis route for a BiOI electrode and its conversion to a highly efficient porous $BiVO_4$ photoanode for solar water oxidation. *Energy Environ. Sci.* **2012**, *5*, 8553–8557.

[8] Kim, T. W.; Choi, K. S. Nanoporous $BiVO_4$ photoanodes with dual-layer oxygen evolution catalysts for solar water splitting. *Science* **2014**, *343*, 990–994.

[9] Kuang, Y. B.; Jia, Q. X.; Nishiyama, H.; Yamada, T.; Kudo, A.; Domen, K. A front-illuminated nanostructured transparent $BiVO_4$ photoanode for >2% efficient water splitting. *Adv. Energy Mater.* **2016**, *6*, 1501645.

[10] Wang, S. C.; Chen, P.; Yun, J. H.; Hu, Y. X.; Wang, L. Z. An electrochemically treated $BiVO_4$ photoanode for efficient photoelectrochemical water splitting. *Angew. Chem., Int. Ed.* **2017**, *56*, 8500–8504.

[11] Kim, C. W.; Son, Y. S.; Kang, M. J.; Kim, D. Y.; Kang, Y. S. (040)-crystal facet engineering of $BiVO_4$ plate photoanodes for solar fuel production. *Adv. Energy Mater.* **2016**, *6*, 1501754.

[12] Han, H. S.; Shin, S.; Kim, D. H.; Park, I. J.; Kim, J. S.; Huang, P. S.; Lee, J. K.; Cho, I. S.; Zheng, X. L. Boosting the solar water oxidation performance of a $BiVO_4$ photoanode by crystallographic orientation control. *Energy Environ. Sci.* **2018**, *11*, 1299–1306.

[13] Wang, S. C.; Liu, G.; Wang, L. Z. Crystal facet engineering of photoelectrodes for photoelectrochemical water splitting. *Chem. Rev.* **2019**, *119*, 5192–5247.

[14] Wang, S. C.; Wang, X.; Liu, B. Y.; Guo, Z. C.; Ostrikov, K. K.; Wang, L. Z.; Huang, W. Vacancy defect engineering of $BiVO_4$ photoanodes for photoelectrochemical water splitting. *Nanoscale* **2021**, *13*, 17989–18009.

[15] Gao, R. T.; Wang, L. Stable Cocatalyst-Free $BiVO_4$ photoanodes with passivated surface states for photocorrosion inhibition. *Angew. Chem., Int. Ed.* **2020**, *59*, 23094–23099.

[16] Feng, S. J.; Wang, T.; Liu, B.; Hu, C. L.; Li, L. L.; Zhao, Z. J.; Gong, J. L. Enriched surface oxygen vacancies of photoanodes by photoetching with enhanced charge separation. *Angew. Chem., Int. Ed.* **2020**, *59*, 2044–2048.

[17] Abdi, F. F.; Han, L. H.; Smets, A. H. M.; Zeman, M.; Dam, B. Van De Krol, R. Efficient solar water splitting by enhanced charge separation in a bismuth vanadate-silicon tandem photoelectrode. *Nat. Commun.* **2013**, *4*, 2195.

[18] Shi, Y. M.; Yu, Y. F.; Yu, Y.; Huang, Y.; Zhao, B. H.; Zhang, B. Boosting photoelectrochemical water oxidation activity and stability of Mo-doped $BiVO_4$ through the uniform assembly coating of NiFe-phenolic networks. *ACS Energy Lett.* **2018**, *3*, 1648–1654.

[19] Kuang, Y. B.; Jia, Q. X.; Ma, G. J.; Hisatomi, T.; Minegishi, T.; Nishiyama, H.; Nakabayashi, M.; Shibata, N.; Yamada, T.; Kudo, A. et al. Ultrastable low-bias water splitting photoanodes via photocorrosion inhibition and *in situ* catalyst regeneration. *Nat. Energy* **2016**, *2*, 16191.

[20] Jin, B. J.; Cho, Y.; Park, C.; Jeong, J.; Kim, S.; Jin, J.; Kim, W.; Wang, L. Y.; Lu, S. Y.; Zhang, S. L. et al. A two-photon tandem black phosphorus quantum dot-sensitized $BiVO_4$ photoanode for solar water splitting. *Energy Environ. Sci.* **2022**, *15*, 672–679.

[21] Ye, S.; Shi, W. W.; Liu, Y.; Li, D. F.; Yin, H.; Chi, H. B.; Luo, Y. L.; Ta, N.; Fan, F. T.; Wang, X. L. et al. Unassisted photoelectrochemical cell with multimediator modulation for solar water splitting exceeding 4% solar-to-hydrogen efficiency. *J. Am. Chem. Soc.* **2021**, *143*, 12499–12508.

[22] Zhang, K.; Jin, B. J.; Park, C.; Cho, Y.; Song, X. F.; Shi, X. J.; Zhang, S. L.; Kim, W.; Zeng, H. B.; Park, J. H. Black phosphorene as a hole extraction layer boosting solar water splitting of oxygen evolution catalysts. *Nat. Commun.* **2019**, *10*, 2001.

[23] Ye, K. H.; Li, H. B.; Huang, D.; Xiao, S.; Qiu, W. T.; Li, M. Y.; Hu, Y. W.; Mai, W.; Ji, H. B.; Yang, S. H. Enhancing photoelectrochemical water splitting by combining work function tuning and heterojunction engineering. *Nat. Commun.* **2019**, *10*, 3687.

[24] Zhou, Y. G.; Zhang, L. Y.; Lin, L. H.; Wygant, B. R.; Liu, Y.; Zhu, Y.; Zheng, Y. B.; Mullins, C. B.; Zhao, Y.; Zhang, X. H. et al. Highly efficient photoelectrochemical water splitting from hierarchical $WO_3/BiVO_4$ nanoporous sphere arrays. *Nano Lett.* **2017**, *17*, 8012–8017.

[25] Hong, S. J.; Lee, S.; Jang, J. S.; Lee, J. S. Heterojunction $BiVO_4/WO_3$ electrodes for enhanced photoactivity of water oxidation. *Energy Environ. Sci.* **2011**, *4*, 1781–1787.

[26] Pihosh, Y.; Turkevych, I.; Mawatari, K.; Uemura, J.; Kazoe, Y.; Kosar, S.; Makita, K.; Sugaya, T.; Matsui, T.; Fujita, D. et al. Photocatalytic generation of hydrogen by core-shell $WO_3/BiVO_4$ nanorods with ultimate water splitting efficiency. *Sci. Rep.* **2015**, *5*, 11141.

[27] Guo, H.; Guo, P. F.; Yang, X. K.; Zhang, J.; Yu, H. W.; Zhao, W. H.; Ye, Q.; Wang, H. Y.; Wang, H. Q. Embedding of WO_3 nanocrystals with rich oxygen-vacancies in solution processed perovskite film for improved photovoltaic performance. *J. Power Sources* **2020**, *461*, 228175.

[28] Zhang, Y. F.; Zhu, Y. K.; Lv, C. X.; Lai, S. J.; Xu, W. J.; Sun, J.; Sun, Y. Y.; Yang, D. J. Enhanced visible-light photoelectrochemical performance via chemical vapor deposition of Fe_2O_3 on a WO_3 film to form a heterojunction. *Rare Met.* **2020**, *39*, 841–849.

[29] Rao, P. M.; Cai, L. L.; Liu, C.; Cho, I. S.; Lee, C. H.; Weisse, J. M.; Yang, P. D.; Zheng, X. L. Simultaneously efficient light absorption and charge separation in $WO_3/BiVO_4$ core/shell nanowire photoanode for photoelectrochemical water oxidation. *Nano Lett.* **2014**, *14*, 1099–1105.

[30] Hanson, E. D.; Lajaunie, L.; Hao, S. Q.; Myers, B. D.; Shi, F. Y.; Murthy, A. A.; Wolverton, C.; Arenal, R.; Dravid, V. P. Systematic study of oxygen vacancy tunable transport properties of few-layer MoO_{3-x} enabled by vapor-based synthesis. *Adv. Funct. Mater.* **2017**, *27*, 1605380.

[31] Balendhran, S.; Deng, J. K.; Ou, J. Z.; Walia, S.; Scott, J.; Tang, J. S.; Wang, K. L.; Field, M. R.; Russo, S.; Zhuiykov, S. et al. Enhanced charge carrier mobility in two-dimensional high dielectric molybdenum oxide. *Adv. Mater.* **2013**, *25*, 109–114.

[32] Chuang, S.; Battaglia, C.; Azcatl, A.; McDonnell, S.; Kang, J. S.; Yin, X. T.; Tosun, M.; Kapadia, R.; Fang, H.; Wallace, R. M. et al. MoS_2 P-type transistors and diodes enabled by high work function MoO_x contacts. *Nano Lett.* **2014**, *14*, 1337–1342.

[33] He, H. C.; Zhou, Y.; Ke, G. L.; Zhong, X. H.; Yang, M. J.; Bian, L.; Lv, K. L.; Dong, F. Q. Improved surface charge transfer in $MoO_3/BiVO_4$ heterojunction film for photoelectrochemical water

oxidation. *Electrochim. Acta* **2017**, *257*, 181–191.

[34] Chen, Y. Q.; Yang, M. J.; Du, J. Y.; Ke, G. L.; Zhong, X. H.; Zhou, Y.; Dong, F. Q.; Bian, L.; He, H. C. MoO_3/$BiVO_4$ heterojunction film with oxygen vacancies for efficient and stable photoelectrochemical water oxidation. *J. Mater. Sci.* **2019**, *54*, 671–682.

[35] Xiao, X.; Zhang, W. D. Facile synthesis of nanostructured BiOI microspheres with high visible light-induced photocatalytic activity. *J. Mater. Chem.* **2010**, *20*, 5866–5870.

[36] Xu, C.; Zou, D. B.; Wang, L. H.; Luo, H.; Ying, T. K. γ-Bi_2MoO_6 nanoplates: Surfactant-assisted hydrothermal synthesis and optical properties. *Ceram. Int.* **2009**, *35*, 2099–2102.

[37] Chandar, N. R.; Agilan, S.; Thangarasu, R.; Muthukumarasamy, N.; Ganesh, R. Influence of the annealing temperature on the formation of $Mo_{17}O_{47}$ and MoO_3 nanoparticles and their Photocatalytic performances for the degradation of MB dye. *J. Mater. Sci. :Mater. Electron.* **2020**, *31*, 7378–7388.

[38] Wang, S. C.; He, T. W.; Yun, J. H.; Hu, Y. X.; Xiao, M.; Du, A. J.; Wang, L. Z. New iron-cobalt oxide catalysts promoting $BiVO_4$ films for photoelectrochemical water splitting. *Adv. Funct. Mater.* **2018**, *28*, 1802685.

[39] Wang, S. C.; He, T. W.; Chen, P.; Du, A. J.; Ostrikov, K. K.; Huang, W.; Wang, L. Z. *In situ* formation of oxygen vacancies achieving near-complete charge separation in planar $BiVO_4$ photoanodes. *Adv. Mater.* **2020**, *32*, 2001385.

[40] Kim, M.; Lee, B.; Ju, H.; Kim, J. Y.; Kim, J.; Lee, S. W. Oxygen-vacancy-introduced $BaSnO_{3-\delta}$ photoanodes with tunable band structures for efficient solar-driven water splitting. *Adv. Mater.* **2019**, *31*, 1903316.

[41] Ning, F. Y.; Shao, M. F.; Xu, S. M.; Fu, Y.; Zhang, R. K.; Wei, M.; Evans, D. G.; Duan, X. TiO_2/graphene/NiFe-layered double hydroxide nanorod array photoanodes for efficient photoelectrochemical water splitting. *Energy Environ. Sci.* **2016**, *9*, 2633–2643.

[42] Silversmit, G.; Depla, D.; Poelman, H.; Marin, G. B.; De Gryse, R. Determination of the V2p XPS binding energies for different vanadium oxidation states (V^{5+} to V^{0+}). *J. Electron Spectrosc. Relat. Phenom.* **2004**, *135*, 167–175.

[43] Jin, S.; Ma, X. X.; Pan, J.; Zhu, C. Y.; Saji, S. E.; Hu, J. G.; Xu, X. Y.; Sun, L. T.; Yin, Z. Y. Oxygen vacancies activating surface reactivity to favor charge separation and transfer in nanoporous $BiVO_4$ photoanodes. *Appl. Catal. B Environ.* **2021**, *281*, 119477.

[44] Zhong, W.; Deng, S. B.; Wang, K.; Li, G. J.; Li, G. Y.; Chen, R. S.; Kwok, H. S. Feasible Route for a Large Area Few-Layer MoS_2 with Magnetron Sputtering. *Nanomaterials (Basel)* **2018**, *8*, 590.

[45] Wang, S. C.; Chen, P.; Bai, Y.; Yun, J. H.; Liu, G.; Wang, L. Z. New $BiVO_4$ dual photoanodes with enriched oxygen vacancies for efficient solar-driven water splitting. *Adv. Mater.* **2018**, *30*, 1800486.

[46] Wang, S. C.; Chen, H. J.; Gao, G. P.; Butburee, T.; Lyu, M.; Thaweesak, S.; Yun, J. H.; Du, A. J.; Liu, G.; Wang, L. Z. Synergistic crystal facet engineering and structural control of WO_3 films exhibiting unprecedented photoelectrochemical performance. *Nano Energy* **2016**, *24*, 94–102.

[47] Ruan, Q. S.; Miao, T. N.; Wang, H.; Tang, J. W. Insight on shallow trap states-introduced photocathodic performance in n-type polymer photocatalysts. *J. Am. Chem. Soc.* **2020**, *142*, 2795–2802.

[48] Huang, H. W.; Cao, R. R.; Yu, S. X.; Xu, K.; Hao, W. C.; Wang, Y. G.; Dong, F.; Zhang, T. R.; Zhang, Y. H. Single-unit-cell layer established Bi_2WO_6 3D hierarchical architectures: Efficient adsorption, photocatalysis and dye-sensitized photoelectrochemical performance. *Appl. Catal. B Environ.* **2017**, *219*, 526–537.